Submitted to *Int. J. Solids & Structures* on July 29th, 2016
Accepted for publication on Dec. 19th, 2016.

Propagation of a height contained hydraulic fracture in turbulent flow regimes

Haseeb Zia, Brice Lecampion

Ecole Polytechnique Fédérale de Lausanne

Geo-Energy Lab, Gaznat chair on Geo-Energy

School of Architecture, Civil & Environmental Engineering

EPFL-ENAC-IIC-GEL, Station 18, Lausanne, CH-1015, Switzerland

November 10, 2016

Abstract

We investigate theoretically and numerically the impact of the transition from laminar to turbulent flow on the propagation of a height contained hydraulic fracture (i.e. PKN geometry). We account for the inertial terms in the balance of momentum and express the viscous wall shear stress via Fanning friction. The evolution of the friction factor with Reynolds number and the fracture relative roughness is obtained for a PKN fracture geometry from known relations for circular pipes using the concept of an equivalent laminar hydraulic diameter. From dimensional analysis, we show that inertial forces are always negligible. We also obtain the transition time scale between the turbulent rough propagation regime -valid at early time- to the turbulent smooth regime. This transition time-scale appears much larger than typical injection duration which confirms the dominant effect of fracture roughness in the turbulent regime. We

derive a number of limiting solutions for hydraulic fracture propagation assuming that the flow occurs in a given regime over all the fracture extent: turbulent smooth or turbulent rough. We then solve numerically the complete laminar to turbulent transition as function of the Reynolds number at the fracture entrance. The fraction of the fracture exhibiting laminar flow shrinks to a boundary layer at the fracture tip as the entrance Reynolds number increases. Our numerical results notably indicate that the entrance Reynolds number must be at least equal to 10,000 for the fully turbulent rough solution to be valid. In practical applications, the entrance Reynolds number is typically lower than 5,000 such that the fracture propagation is influenced by the complete transition from laminar to turbulent flow. Using our numerical scheme, we tabulate the evolution of the fracture length and width at the fracture entrance for different values of the entrance Reynolds number covering the transition from the fully laminar to the fully turbulent rough regime. The effect of polymer friction reducing agents, which drastically modify the transition to turbulence, is also investigated semi-analytically and numerically. The height contained hydraulic fracture propagation (assuming maximum drag reduction) is only about 15% different from the fully laminar solution in the range of relevant practical entrance Reynolds number, compared to up to 40% difference without the addition of polymer friction reducers.

1 Introduction

The use of high injection rate water-based hydraulic fracturing has been highly successful in unlocking gas production from extremely low permeability unconventional reservoirs. A given pumping operation (a "stage") usually aims at propagating simultaneously several hydraulic fractures along a well interval - the preferred initiation point being controlled via perforations. In order to compensate the negative effect of the low viscosity of water on the settling of proppant, very large injection rate are typically used: up to 120 barrels per minute ($0.318\,\mathrm{m}^3/\mathrm{s}$) in the case where multiple fractures (from four to eight typically) are

driven simultaneously. It is now recognized that not all fractures are successfully propagated during a pumping operation (Lecampion et al., 2015; Lecampion and Desroches, 2015). As a result, the injection rate entering a given fracture can be as large as 40 Barrels per minutes. Such a large fluid injection rate clearly questions the classical hypothesis of laminar flow in a propagating hydraulic fracture (Economides and Nolte, 2000; Detournay, 2016). Neglecting the occurence of turbulent flow in part of the fracture may result in a wrong estimation of the evolution of fracture length, width and pressure with time. In order to investigate the deviation from the fully laminar flow assumption, we focus our discussion on the simple yet practically relevant geometry of a bi-wing height contained hydraulic fracture (see Fig. 1). Such a fracture geometry develops when a reservoir layer of height h is bounded (top and bottom) by higher stressed layers. In that case, the average velocity of the fluid is $\bar{v} = Q_o/(2h\,\bar{w})$ where $\bar{w}$ is the average fracture width, $Q_o/2$ is the rate entering one wing of the fracture and h is the reservoir height. Taking the average width as the flow dimension, the Reynolds number defined as $\rho\bar{v}\bar{w}/\mu$ for flow in the fracture becomes $\mathcal{R} = \rho Q_o/(2h\mu)$, with ρ and μ the fracturing fluid density and viscosity. Taking realistic values for the reservoir properties (see Table 1), the Reynolds number can exceed the critical value above which turbulent flow occurs for large - but realistic- value of the injection rate entering the fracture (see Table 2). In fact, varying the reservoir parameters and injection rate in a realistic range, we observe that for a height contained hydraulic fracture, the Reynolds number $\mathcal{R}$ falls in the range $10^3 - 10^4$.

Investigations of the effect of turbulent flow on hydraulic fracture propagation can be traced back to the work of Nilson (1981) for the case of a plane-strain fracture driven by gas injection. Limiting turbulent flow regimes were also explored for the problem of buoyancy-driven propagation of magmatic dikes (Spence and Turcotte, 1990; Lister and Kerr, 1991). More recently, a solution for hydraulic fracture propagation at glacier beds in the fully rough turbulent regime was obtained for a plane-strain fracture (Tsai and Rice, 2010). For the type of conditions encountered at glacier beds, the Reynolds numbers are above 10^5 for which the

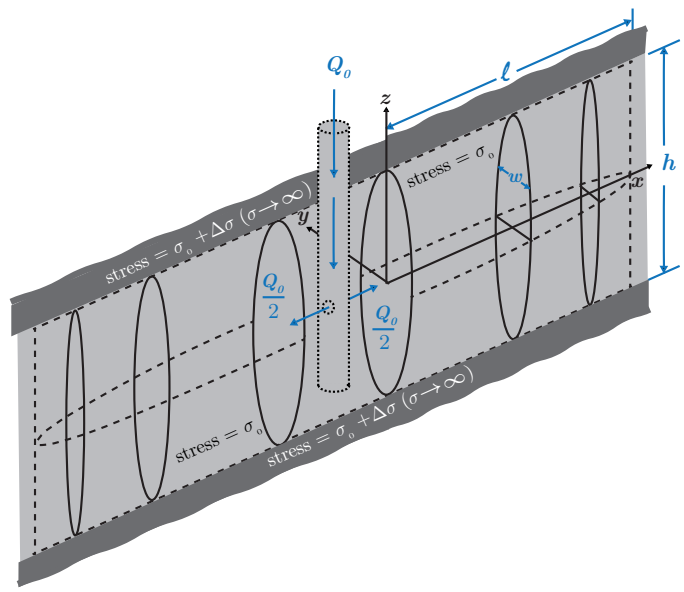

Figure 1: Sketch of a bi-wing height-contained (PKN) hydraulic fracture of half-length ℓ, width w and constant height h.

flow is completely governed by the fracture relative roughness, i.e. the rough turbulent regime governed by the Gauckler-Manning-Strickler formula (see Fig.2). Ames and Bunger (2015) have derived scaling laws for the propagation of a height contained fracture in the same fully turbulent rough regime. Rough turbulent flow appears to result in shorter fracture length and larger fracture width compared to the laminar flow case. How accurate is the approximation of a fully rough turbulent flow in all the fracture remains however unclear for practical cases where $\mathcal{R} \in [10^3 - 10^4]$. All of these contributions have assumed a single flow regime (e.g. turbulent rough) over the entire fracture extent. However, as noted by Nilson (1981), the flow remains laminar close to the fracture tip as the fracture width goes to zero (and so is the local value of Reynolds number). In other words, a transition from turbulent to laminar flow will occur as one moves close to the fracture tip - even for large value of the entrance Reynolds number $\mathcal{R}$ for which the laminar region will shrink to a boundary layer near the fracture tip.

In this paper, focusing on the height contained fracture geometry (Fig.1), we investigate the complete transition from laminar to turbulent flow accounting for both the effects of

Parameter	Value
ρ	1000kg/m^3
μ	1.3×10^{-3}Pa s
h	10m
E'	32 GPa
k	1 mm

Table 1: Fracturing fluid properties (density, viscosity) for water, and realistic values of rock properties (plane strain Young's modulus E', fracture roughness lengthscale k which is order of the rock grain size) and fracture height h (see e.g. Economides and Nolte (2000)). The fracture heigth typically corresponds to the height of the reservoir layer.

the Reynolds number and relative roughness on the friction factor. We review the available experimental data and models for the evolution of the friction factor covering the different flow conditions from laminar to fully turbulent. A dimensional analysis of the governing equations of hydraulic fracture propagation provides a useful understanding of the structure of the solution in different flow regimes as well as the transition between these regimes. We also derive a number of semi-analytical solutions for limiting flow regimes: e.g. fully turbulent rough or fully turbulent smooth. The complete transition between the laminar and turbulent regimes is investigated numerically using a model for the friction factor properly reproducing the available experimental data over the full range of Reynolds numbers and relative roughness (Yang and Dou, 2010). Comparisons of our numerical results with the solutions for the different limiting flow regimes notably enable to quantify the range of these limiting solutions. We finally explore the effect of the addition of friction reducers in the injected water. These polymer additives are well known to significantly change the transition to turbulence even at small concentrations (Virk, 1975). Here again, we derive a semi-analytical solution in the limiting regime of full maximum drag reduction and explore the complete transition from laminar flow numerically.

Q_0 (bbl/min)	Q_0 (m^3/s)	$\mathcal{R} = \dfrac{\rho Q_o}{2h\mu}$
10	0.026	1000
20	0.053	2038
30	0.079	3038
40	0.106	4077

Table 2: Inlet Reynolds number $\mathcal{R}$ in a height contained fracture evaluated with the parameters listed in Table 1 for different values of injection rate. Transition to turbulent flow starts at $\mathcal{R}_c \approx 1380$ for such a fracture geometry (see section 2.2.2).

2 Problem formulation

We focus on the case of a height contained hydraulic fracture of half-length ℓ growing under the injection of a Newtonian fluid of viscosity μ and density ρ at a constant rate Q_o. The fracture is assumed to grow symmetrically from the line source of fluid injection. We thus perform the analysis only on one-half (i.e. one wing) of the fracture. Such a geometry -often called the PKN geometry in reference to the original work of Perkins, Kern and Nordgren (Perkins et al., 1961; Nordgren, 1972)- corresponds to the case of a hydraulic fracture propagating in a rock layer of height h whose in-situ minimum compressive stress σ_o is lower than the stress of the top and bottom adjacent layers $\sigma_o + \Delta\sigma$ ($\Delta\sigma > 0$). Assuming an infinite stress contrast ($\Delta\sigma \to \infty$) between the middle and adjacent layers, the hydraulic fracture is strictly contained in the middle layer (see Fig. 1). The PKN model assumes a one dimensional growth horizontally (along the x axis in Fig. 1). As a result, the fracture height h is constant (equal to the layer height) and the fluid flow is unidimensional (the fluid pressure is uniform vertically at a given cross-section along the x axis).

2.1 Elasticity

The PKN model assumes that the fracture length is much greater than its height, $\ell \gg h$, and simplify the elastic deformation of the fracture by assuming an independent state of plane-strain at each cross section along x-axis: i.e. the fluid pressure at $x = x_a$ does not influence the fracture shape at $x = x_b$. Such a "local elasticity" hypothesis is valid away from the

fracture tip when $\ell \gg h/2$ (see Adachi and Peirce (2008) for more details). At a given x, the fracture is in a state of plane-strain under a uniform net pressure $p(x,\, t) = p_f(x,t) - \sigma_o$ which is equal to the excess of fluid pressure p_f above the minimum in-situ stress σ_o. Assuming that the rock is homogeneous and isotropic, the width of the fracture is given by the solution of a uniformly pressurized crack under plane-strain conditions (Sneddon and Elliot, 1946):

$$w(x,z,t) = \frac{2h\,p(x,t)}{E'}\sqrt{1-\frac{4z^2}{h^2}}, \tag{1}$$

where $E' = E/(1-\nu^2)$ is the plane-strain modulus of the rock, E and ν are the Young's modulus and Poisson's ratio respectively. The fracture width has an elliptical profile at a given x along the fracture propagation axis. The model assumes uni-dimensional flow and we will thus make use of the averaged fracture width $\overline{w}$ for a given cross section (Sarvaramini and Garagash, 2015):

$$\overline{w}(x,t) = \frac{1}{h}\int_{-h/2}^{h/2} w(x,z,t)\mathrm{d}z = \frac{\pi}{4}\frac{2hp(x,t)}{E'} = \frac{\pi}{4}w(x,0,t)\ . \tag{2}$$

The fluid pressure is directly related to the averaged width (local elasticity). In the original PKN model, the energy required to fracture the rock is essentially neglected. The net pressure and fracture width are set to zero at the fracture tip:

$$\overline{w}(x=\ell,\, t) = p(\ell,t) = 0 \tag{3}$$

The effect of fracture toughness can be included in the model keeping the one-dimensional character of the geometrical configuration as discussed in Sarvaramini and Garagash (2015) (see also Dontsov and Peirce (2015) for a discussion on the incorporation of fracture toughness in such a model). In the following, we neglect fracture energy in line with the original hypothesis of the PKN model.

2.2 Fluid flow

As already mentioned, the fluid flow is uni-dimensional and we denote $v_x = v$ as the only non-zero component of the fluid velocity vector. Neglecting the fracturing fluid compressibility compared to the fracture compliance (a hypothesis verified for any fracturing liquid), the local mass conservation reduces to the following continuity equation at a given cross section located at x:

$$\frac{\partial A(x,t)}{\partial t} + \frac{\partial Q(x,t)}{\partial x} = 0, \tag{4}$$

where $A(x,t) = \overline{w}(x,t)h$ is the cross-sectional area of the fracture in the y-z plane at x and $Q(x,t) = A(x,t)\overline{v}$ is the fluid flow rate equals to the cross section area times the average fluid velocity $\overline{v}$ in the x-direction. For clarity of our discussion on the effect of turbulent flow, we assume an impermeable rock and thus neglect any leak off of the fracturing fluid into the surrounding rock.

The fluid is injected at $x = 0$ into the bi-wing fracture under a constant flow rate Q_0. The flow rate entering one wing of the fracture is thus simply:

$$Q(x = 0, t) = \frac{Q_0}{2} \tag{5}$$

The fluid flow rate is zero at the fracture tip ($x = \ell$) which provides the following boundary condition (in addition to Eq. (3)):

$$Q(x = \ell, t) = 0 \tag{6}$$

2.2.1 Balance of Momentum

Similarly than for mass conservation, we write the cross-sectional average of the fluid momentum equation:

$$\rho\left(\frac{\partial Q}{\partial t}+\frac{\partial Q\overline{v}}{\partial x}\right)=-A\frac{\partial p}{\partial x}-\text{Þ}\tau_w,$$

where Þ is the perimeter of the cross-section of area A and τ_w is the average wall shear stress typically expressed as:

$$\tau_w=f\frac{\rho\overline{v}^2}{2}.$$

Here, f is the Fanning friction factor which depends on the Reynolds number, the relative roughness of the flow geometry and the shape of the cross-section perpendicular to the flow direction. Strictly speaking, the model / experimental results for the friction factor are all based on the assumption of a unidirectional steady developed flow. They are therefore inadequate for un-steady flow. However, as we shall see when performing the dimensional analysis of the problem, the inertial terms appearing on the left hand side of the balance of momentum are always negligible in our case, justifying the use of a local steady wall-shear stress model at any cross section along the fracture. The friction factor f will evolve spatially along the fracture as the local Reynolds number and relative roughness of the fracture depends on the local values of mean width $\overline{w}$ and mean velocity $\overline{v}$.

Using the continuity equation (4), the balance of momentum can be re-written as:

$$\rho\left(\frac{\partial\overline{v}}{\partial t}+\overline{v}\frac{\partial\overline{v}}{\partial x}\right)=-\frac{\partial p}{\partial x}-\frac{\text{Þ}}{A}f\frac{\rho\overline{v}^2}{2}. \tag{7}$$

The solution of the problem entails to obtain the time evolution of the fracture half-length, mean fracture width, net pressure and mean fluid velocity as fluid is injected continuously at the origin. This problem is governed by the elastic relation (2), the fluid continuity (4) and balance of momentum equations (7), boundary conditions (3) and (5)-(6) together with an expression for the variation of the friction factor f with the local value of the Reynolds

number and relative fracture roughness.

2.2.2 Evolution of the friction factor

The evolution of the friction factor as function of the Reynolds number and relative roughness is well known for circular pipes. The classical experiments of Nikuradse (1950) in smooth and rough circular pipes have notably provided the basis for a number of relations for the evolution of the friction factor (see Fig. 2). In order to use these relations for a non-circular flow section, the hydraulic diameter $D_h = 4A/\text{Þ}$ is often taken to replace the pipe diameter in the definition of the Reynolds number. However, experimental studies have shown that the obtained predictions are inaccurate (Sadatomi et al., 1982; Carlson and Irvine, 1961; Jones, 1976). In place of the hydraulic diameter, Jones (1976) suggests to obtain the characteristic dimension of the flow D_{eq} by matching the laminar friction of the non-circular cross section (which can be obtained analytically for most cross-section as function of its dimensions) with the expression for a circular pipe in the laminar flow regime $f = 16/Re_{D_{eq}}$. The predictions of friction in the turbulent regime using $Re_{D_{eq}}$ instead of Re_{D_h} in the expressions for a circular pipe then agrees well with experimental data for rectangular ducts (Jones, 1976).

In our case, the cross-section of the flow has an elliptical shape due to the elastic relation (1). The uni-dimensional pressure-driven laminar flow across an ellipse of semi-axes $h/2$ and $w(0)/2 = 2\overline{w}/\pi$ is well-known (see e.g. Lamb (1895)). In the case of a fracture of height h much larger than its mean width $\bar{w}$, the mean laminar velocity reduces to:

$$\overline{v} = -\frac{1}{\pi^2}\frac{\overline{w}^2}{\mu}\frac{\partial p}{\partial x}$$

Writing $f = 16/Re_{D_{eq}} = 16\mu/(\rho D_{eq}\overline{v})$ in the laminar regime where inertial terms are negligible, the balance of momentum combined with the previous solution for the mean velocity gives the following "laminar pipe equivalent" characteristic scale for a thin elliptical cross-

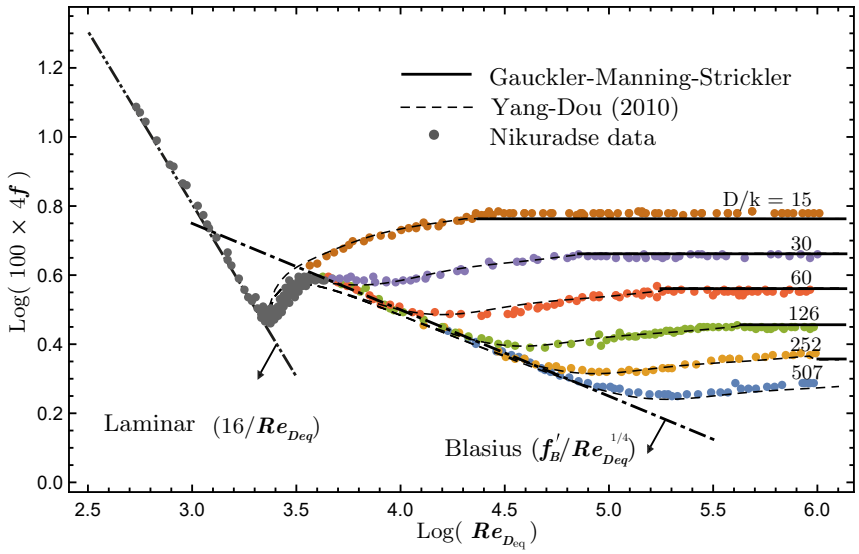

Figure 2: Evolution of the friction factor f in circular pipe as function of the Reynolds number $Re_{D_{eq}} = \rho\bar{v}D/\mu$ and relative roughness $\epsilon = (2k/D)$, where k is the characteristic roughness scale (and $D/2$ the pipe radius). The experimental data of Nikuradse (1950) for pipes of different roughness are plotted together with the expressions for the laminar friction $f = 16/Re_{D_{eq}}$ valid for $Re_{D_{eq}} < 2300$, the smooth turbulent Blasius friction $4f = 0.316Re^{-1/4}$ (dash-dotted black line) and the turbulent rough Glaucker-Manning-Strickler $4f = 0.143(2k/D)^{1/3}$ (solid black line). The predictions of the model of Yang and Dou (2010) are also plotted as thin dashed lines and follow the experimental data closely.

section:

$$D_{eq} = \frac{5}{\pi}\overline{w}$$

We will therefore use the expressions of the friction factor for circular pipes with D_{eq} as an equivalent pipe diameter. In other words, following Jones (1976), we will use the following definition for the equivalent laminar pipe Reynolds number $Re_{D_{eq}}$:

$$Re_{D_{eq}} = \frac{5}{\pi}Re, \tag{8}$$

where $Re = \rho\overline{w}\,\overline{v}/\mu$ corresponds to the Reynolds number defined with the mean fracture width as the characteristic flow dimension. Such a choice allows to use the different friction models derived for circular pipe for the case of an elliptical cross-section while ensuring that we recover the same friction in the laminar regime. As can be seen in Fig. 2, the transition to turbulent flow occurs at $Re_D \approx 2200$ in pipe, which gives a critical number $\mathcal{R}_c \approx 2200 \times \pi/5 \approx 1380$ for our flat elliptical cross-section - a value consistent with the order of magnitude for a plane Poiseuille flow. It is however important to realize that the transition to turbulence can occur over a large range of Reynolds number. One should use the estimate of this critical Reynolds number with care, especially knowing the spatio-temporal effects associated with the transition to turbulence (Manneville, 2016).

In the following, we aim to model the effect of the complete dependence of the friction factor on Reynolds number and relative roughness on fracture propagation. A large number of empirical and theoretical formulae have been proposed over the years to model the data represented in Fig. 2. Notably, the turbulent regime for smooth pipes is well captured by the Blasius (1913) scaling (see Fig. 2) :

$$f = f'_B Re_{D_{eq}}^{-1/4}, \qquad f'_B = 0.316/4 \tag{9}$$

which is an empirical formula with a response similar to the Prandtl-Karman theoretical

predictions for smooth pipe. Note that the factor 4 in f'_B stems from our use of the Fanning definition of the friction factor compared to the Darcy-Weisbach definition.

At very large Reynolds number ($Re \gtrsim 10^5$), friction is governed solely by the relative roughness of the pipe $\epsilon = k/R = 2k/D$ where k is the roughness lengthscale (and $R = D/2$ the pipe radius). In that rough turbulent limiting regime, the friction factor evolves according to the Gauckler-Manning-Strickler (G-M-S) scaling $f = \dfrac{0.143}{4}\epsilon^{1/3}$. For our case where the flow occurs through a thin elliptical cross-section, different value of the relative roughness could be used. In line with the use of an equivalent laminar diameter D_{eq} to capture the dependence of f with Re, one could use the same scale to define a relative roughness $\epsilon = 2k/D_{eq} = 2\pi k/(5\overline{w})$ as suggested by Jones (1976). On the other hand, another choice is to simply use the mean fracture width to define the relative roughness as $\epsilon = 2k/\overline{w}$. Unfortunately, we have not found any good experimental data set for turbulent flow in rough rectangular duct that could help deciphering between these two choices. We settle for the definition of the relative roughness as $\epsilon = 2k/\overline{w}$. Note that the relative roughness is sometimes written as $\kappa/\overline{w}$ (e.g. Tsai and Rice (2010); Ames and Bunger (2015)), however, in order to match Nikuradse data with the prefactor 0.143/4, κ must then be defined as twice the roughness lengthscale. In what follow, we write the friction factor as:

$$f = f'_R \times \left(\frac{k}{\overline{w}}\right)^{1/3} \qquad f'_R = 2^{1/3} \times 0.143/4 \tag{10}$$

in that fully rough turbulent regime (see Fig.2). One can note that when introduced in the previous relation (10) for friction, the relative difference between the two choice of relative roughness ($2k/D_{eq}$ vs $2k/\overline{w}$) is of approximately $1 - (\pi/5)^{1/3} = 14\%$.

A number of empirical or semi-theoretical models have been proposed to capture the dependence of the friction factor on both Reynolds number and relative roughness over the full range of Re and ϵ. In the following, we use the semi-theoretical modef proposed by Yang and Dou (2010) although similar results would be obtained with any other model properly

reproducing Nikuradse data (e.g. Yang and Joseph (2009); Li and Huai (2016)). We will also obtain semi-analytical solutions for some limiting cases by assuming that friction can be modeled via the Blasius (9) or the rough turbulent (10) scaling over the entire range of $Re_{D_{eq}}$. We will refer to these limiting solutions as turbulent smooth and turbulent rough respectively.

3 Dimensional analysis and scaling

The propagation of a PKN fracture is known to be self-similar in the case of laminar flow (Perkins et al. (1961); Nordgren (1972)). The solution can then be obtained semi-analytically (Kemp et al., 1990). Our aim is to investigate departure from such a laminar case. In order to grasp the structure of the solution of the problem, let us introduce some characteristics scales W_*, P_*, V_* and L_* (possibly time-dependent) for the fracture width, pressure, propagation velocity and length respectively. Scaling the spatial coordinate x by the fracture length $\ell(t)$, $\xi = x/\ell(t)$, we write the following scaling for fracture length, mean fracture width, net pressure and fluid velocity respectively:

$$\begin{aligned}
\ell &= L_*\gamma(\mathcal{G}_1,\, \mathcal{G}_2...), \\
\overline{w} &= W_*\Omega(\xi; \mathcal{G}_1,\, \mathcal{G}_2...), \\
p &= P_*\Pi(\xi; \mathcal{G}_1,\, \mathcal{G}_2...), \\
\overline{v} &= V_*\Upsilon(\xi, \mathcal{G}_1,\, \mathcal{G}_2...).
\end{aligned} \tag{11}$$

The dimensionless fracture length γ, opening Ω, net pressure Π and mean fluid velocity Υ may depend on a number of dimensionless parameters $\mathcal{G}_1$, $\mathcal{G}_2$ etc. besides the dimensionless spatial coordinate $\xi = x/\ell(t)$. Introducing the previous scaling in the governing equations will allow to define the different characteristic scales and dimensionless parameters. First,

the "laminar-equivalent" Reynolds number $Re_{D_{eq}}$ (8) takes the following form:

$$Re_{D_{eq}} = \frac{5}{\pi} \underbrace{\frac{\rho W_* V_*}{\mu}}_{\mathcal{R}} \Omega \Upsilon.$$

where $\mathcal{R} = \rho W_* V_* / \mu$ is a characteristic Reynolds number. The elastic relation (2) for the mean width now gives:

$$\Omega = \underbrace{\frac{\pi}{2} \frac{h P_*}{E' W_*}}_{\mathcal{G}_e} \Pi \tag{12}$$

while the inlet ($\xi = 0$) (5) and tip ($\xi = 1$) (3)-(6) boundary conditions reduce to:

$$\begin{aligned} \Omega(\xi = 0)\Upsilon(\xi = 0) &= \underbrace{\frac{Q_o}{2h\, W_* V_*}}_{\mathcal{G}_q} \\ \Omega(\xi = 1) = \Pi(\xi = 1) &= 0 \\ \Omega(\xi = 1)\Upsilon(\xi = 1) &= 0 \end{aligned} \tag{13}$$

The dimensionless form of the continuity equation is obtained as[1]:

$$t\partial_t \Omega + \frac{\dot{W}_*}{W_*} t\Omega - \xi \left(\frac{\dot{L}_* t}{L_*} + \frac{\dot{\gamma}}{\gamma} t \right) \partial_\xi \Omega + \underbrace{\frac{V_* t}{L_*}}_{\mathcal{G}_v} \frac{1}{\gamma} \partial_\xi \left(\Omega \Upsilon \right) = 0. \tag{14}$$

Similarly, noting that $A/\text{Þ} = 8\overline{w}/5\pi$ for the PKN fracture geometry, the momentum equation (7) can be re-written as

$$\frac{\rho W_* V_*}{\mu} \left(t\partial_t \Upsilon - \left(\frac{\dot{L}_* t}{L_*} + \frac{\dot{\gamma} t}{\gamma} \right) \xi \partial_\xi \Upsilon + \frac{V_* t}{L_*} \frac{\Upsilon}{\gamma} \partial_\xi \Upsilon \right) =$$

[1]With the changes of variable $\xi = x/\ell(t)$, the temporal and spatial derivatives are given by:

$$\partial_t|_x = \partial_t|_\xi - \frac{\dot{\ell}}{\ell} \xi \partial_\xi \qquad \partial_x = \frac{1}{\ell} \partial_\xi.$$

$$-\frac{W_* P_* t}{\mu L_*}\frac{1}{\gamma}\partial_\xi \Pi - \frac{5\pi}{16}\frac{\rho V_*^2 t}{\mu} \times f(Re_{D_{eq}}, \frac{k}{W_*\Omega}) \times \frac{\Upsilon^2}{\Omega},$$

which after multiplication by $\mathcal{G}_\epsilon = \frac{W_*}{V_* t}$ and division by $5\pi\mathcal{R}/16$ can be further re-written as:

$$\begin{aligned} \frac{16}{5\pi}\mathcal{G}_\epsilon \left(t\partial_t \Upsilon - \left(\frac{\dot{L}_* t}{L_*} + \frac{\dot{\gamma} t}{\gamma} \right) \xi \partial_\xi \Upsilon + \mathcal{G}_v \frac{\Upsilon}{\gamma}\partial_\xi \Upsilon \right) &= \\ -\underbrace{\frac{16}{5\pi\mathcal{R}}\frac{W_*^2 P_*}{\mu L_* V_*}}_{\mathcal{G}_p}\frac{1}{\gamma}\partial_\xi \Pi - f(\frac{5}{\pi}\mathcal{R} \times \Omega\Upsilon, \underbrace{\frac{k}{W_*}}_{\mathcal{G}_r}\frac{1}{\Omega}) \times \frac{\Upsilon^2}{\Omega} &, \end{aligned} \tag{15}$$

where we have highlighted the dependence of the friction factor f on $Re_{D_{eq}} = \frac{5}{\pi}\mathcal{R}\Omega\Upsilon$ and the relative roughness $\epsilon = k/(W_*\Omega) = \mathcal{G}_r/\Omega$.

In summary, the following dimensionless groups appears in the dimensionless system of equations:

$$\mathcal{G}_e = \frac{\pi}{2}\frac{hP_*}{E'W_*}, \qquad \mathcal{G}_v = \frac{V_* t}{L_*}, \qquad \mathcal{G}_\epsilon = \frac{W_*}{V_* t}, \qquad \mathcal{G}_q = \frac{Q_o}{2hW_*V_*},$$
$$\mathcal{G}_p = \frac{16}{5\pi\mathcal{R}}\frac{W_*^2 P_*}{\mu L_* V_*}, \qquad \mathcal{G}_r = \frac{k}{W_*} \qquad \mathcal{R} = \frac{\rho W_* V_*}{\mu}$$

In order to obtain dimensionless quantities (e.g. Ω, Π, Υ) of order one, it is natural to set the dimensionless groups $\mathcal{G}_e$, $\mathcal{G}_q$ appearing in the elastic relation (12) and inlet flux boundary condition (13) to unity respectively. Similarly, the fracture lengthscale L_* should scale with respect to the characteristic velocity, i.e. $L_* = V_* t$ ($\mathcal{G}_v = 1$). In doing so, we can express the characteristic velocity, opening and pressure scales solely as function of L_*

$$V_* = L_*/t \qquad W_* = \frac{Q_o t}{2hL_*} \qquad P_* = \frac{2E'W_*}{\pi h} = \frac{E'}{\pi\, h^2}\frac{Q_o t}{L_*} \tag{16}$$

and the remaining non-zero dimensionless numbers are

$$\mathcal{G}_\epsilon = \frac{W_*}{L_*} = \frac{Q_o t}{2hL_*^2} \qquad \mathcal{G}_p = \frac{8}{5\pi^2}\frac{E'Q_o^2 t^4}{\rho h^3 L_*^5} \qquad \mathcal{G}_r = \frac{2khL_*}{Q_o t} \qquad \mathcal{R} = \frac{\rho Q_o}{2h\mu}$$

The fracture characteristic lengthscale L_* remains to be defined in order to complete the definition of the scaling. Before doing so, a number of interesting points can already be made. Due to the inlet flux boundary conditions, the characteristic Reynolds number $\mathcal{R}$ (times the geometrical factor $5/\pi$) corresponds to the entrance value of $Re_{D_{eq}}$, i.e. the maximum value of the Reynolds number encountered inside the fracture. It corresponds exactly to the expression obtained from simplified considerations in the Introduction. The characteristic width W_* of a fracture is always much smaller than its characteristic length L_*, i.e. $\mathcal{G}_\epsilon \ll 1$. The inertial terms (left-hand side of the balance of momentum) are factored by $\mathcal{G}_\epsilon$, and are thus always negligible compared to the friction and pressure gradient terms for such type of flow.

3.1 Scalings

In order to define the characteristic fracture lengthscale L_*, one needs to balance the order of magnitude of the pressure gradient and friction terms in the balance of momentum. We thus need to introduce the dependence of the friction factor as function of the Reynolds number and the relative roughness. Different scalings relevant for different flow regimes (laminar vs turbulent smooth or turbulent rough) can thus be obtained. In fact, two distinct scalings emerge.

Laminar - turbulent smooth scalings In the first type of scalings, the friction factor is assumed to be independent of relative roughness and decays as a power law of Reynolds number i.e $f = f' Re^{-\beta}$. This is the case for the laminar regime ($f' = 16$, $\beta = 1$) as well as the turbulent smooth Blasius-type scaling ($f' = f'_B, \beta = 1/4$) - and in fact other scalings for the case of polymer drag reducing agents as we shall see later. Introducing

	L_*	W_*	$\mathcal{G}_\epsilon = W_*/L_*$
Laminar	$\frac{E'^{1/5}Q_0^{3/5}t^{4/5}}{2^{2/5}\pi^{3/5}h^{4/5}\mu^{1/5}}$	$\frac{\pi^{3/5}\mu^{1/5}Q_0^{2/5}t^{1/5}}{2^{3/5}E'^{1/5}h^{1/5}}$	$\frac{\pi^{6/5}h^{3/5}\mu^{2/5}}{2^{1/5}E'^{2/5}Q_o^{1/5}t^{3/5}}$
Turbulent smooth	$\frac{2^{11/20}}{5^{3/20}\pi^{9/20}}\frac{E'^{1/5}Q_o^{9/20}t^{4/5}}{f_B'^{1/5}h^{13/20}\mu^{1/20}\rho^{3/20}}$	$\frac{5^{3/20}\pi^{9/20}}{2\times 2^{11/20}}\frac{f_B'^{1/5}\mu^{1/20}Q_o^{11/20}\rho^{3/20}t^{1/5}}{E'^{1/5}h^{7/20}}$	$\frac{\pi^{9/10}5^{3/10}}{4\times 2^{1/10}}\frac{h^{3/10}\mu^{1/10}\rho^{3/10}Q_o^{1/10}}{E'^{2/5}t^{3/5}}$
Turbulent rough	$\frac{\sqrt{2}E'^{3/16}Q_0^{7/16}t^{13/16}}{5^{3/16}\pi^{3/8}f_R'^{3/16}h^{5/8}k^{1/16}\rho^{3/16}}$	$\frac{5^{3/16}f_R'^{3/16}k^{1/16}\pi^{3/8}Q_0^{9/16}\rho^{3/16}t^{3/16}}{2\sqrt{2}E'^{3/16}h^{3/8}}$	$\frac{5^{3/8}\pi^{3/4}f_R'^{3/8}h^{1/4}k^{1/8}Q_o^{1/8}\rho^{3/8}}{4E'^{3/8}t^{5/8}}$

Table 3: Characteristic fracture length and width in the different scalings (the characteristic pressure and velocity can be easily obtained from Eq. (16)). The dimensionless number $\mathcal{G}_\epsilon = W_*/L_*$ controls the (negligible) intensity of inertia. In the general case, where friction is function of both roughness and Reynolds number, the dimensionless solution depends on the fracture entrance Reynolds number $\mathcal{R} = (Q_o\rho)/(2h\mu)$ and dimensionless roughness $\mathcal{G}_r = k/W_*$.

$f = f'Re_{D_{eq}}^{-\beta} = f' \times \left(\frac{5}{\pi}\mathcal{R}\Omega\Upsilon\right)^{-\beta}$ in (15), balancing $\mathcal{G}_p$ with $f' \times \left(\frac{5}{\pi}\mathcal{R}\right)^{-\beta}$, we obtain

$$L_\beta = \frac{2^{(3-\beta)/5}}{5^{(1-\beta)/5}\pi^{(\beta+2)/5}}\frac{E'^{1/5}Q_o^{(\beta+2)/5}\rho^{(\beta-1)/5}t^{4/5}}{f'^{1/5}\mu^\beta h^{(3+\beta)/5}}$$

Table 3 lists the different characteristic scales as well as the remaining dimensionless number $\mathcal{G}_\epsilon$ for the laminar and turbulent smooth Blasius regime. As expected, we exactly recover the scaling of the original PKN solution for the laminar case (Nordgren, 1972).

Turbulent rough scaling The second type of scaling corresponds to the rough turbulent regime where friction only depends on the relative roughness: $f = f_R' \times (k/\overline{w})^{1/3}$. Again after introduction in the dimensionless balance of momentum and balancing the pressure gradient and friction terms, we obtain:

$$L_R = \frac{\sqrt{2}E'^{3/16}Q_0^{7/16}t^{13/16}}{5^{3/16}\pi^{3/8}f_R'^{3/16}h^{5/8}k^{1/16}\rho^{3/16}}$$

Such a scaling also listed in Table 3 corresponds to the one derived in Ames and Bunger (2015) (pending a numerical factor $2^{1/3}$ associated with the definition of the G-M-S pre-factor

f'_R in that reference).

Discussion It is worth re-iterating that the inertial terms which are factored by $\mathcal{G}_\epsilon$ in the balance of momentum equation are always negligible. In fact, as can be seen from Table 3, $\mathcal{G}_\epsilon$ decays with time. Inertial effects may thus only be relevant at very short time-scales. To illustrate this point, in the turbulent rough case, we can easily obtain the time for which $\mathcal{G}_\epsilon = 10^{-3} \ll 1$ for a given set of problem parameters. Using the values listed in Table 1, an injection rate of $0.079\text{m}^3/\text{s}$ (30bbl/min) and the expression of $\mathcal{G}_\epsilon$ for the rough scaling (see Table 3), we obtain a value of 0.13 seconds. For injection time larger than this value, inertial effects will have a negligible role. The dimensionless solution of the problem then only depends on the characteristic Reynolds number $\mathcal{R}$ and the relative roughness $\mathcal{G}_r$. From now on, we will only focus on the case of negligible inertia ($\mathcal{G}_\epsilon = 0$). Note that in the case of gas fracturing, the time at which inertial effects vanishes may be much larger (see e.g. Nilson (1981)).

The scalings in Table 3 also confirm the physical intuition that the relative roughness decreases with time as it scales as k/W_* and the characteristic width increases with time. Therefore, referring to Fig. 2 displaying the evolution of the friction factor with Re and ϵ, we see that - if in the turbulent regime - the flow inside the fracture will be governed by roughness at early time and will transition -as the fracture width increases and the relative roughness decreases - toward the smooth turbulent regime governed by Blasius scaling. We can obtain an estimate of the time-scale of such a transition by finding the time t at which the characteristic lengthscale L_* of the turbulent rough and turbulent smooth scalings are equal. Dropping the numerical constants of order one, we obtain from Table 3:

$$t_{R\to S} = \frac{E' f_R'^{15} k^5 \rho^2}{f_B'^{16} h \mu^3} \mathcal{R}. \tag{17}$$

Using an injection rate of rate of $0.079\text{m}^3/\text{s}$ (30bbl/min) and parameters from Table 1 realistic for a high rate water fracturing treatment, we obtain $t_{R\to S} \approx 1.22 \times 10^{10}$ seconds. This

indicates that if turbulent, the flow will not reach the limiting regime of turbulent smooth propagation during the typical duration of an injection (between one to three hours).

3.2 Solutions for limiting regimes

If one assumes that the friction factor evolves as $f = f' Re_{D_{eq}}^{-\beta}$ or alternatively as $f = f'_R \times (k/\overline{w})^{1/3}$, the dimensionless system of equations do not depend on any other dimensionless parameters (neglecting inertia) in the corresponding scalings. The solutions are therefore self-similar: the evolution of length, width etc. are given by the power-law scalings in Table 3. It is possible to obtain a semi-analytical solution for the dimensionless fracture width profile $\Omega(\xi)$ and dimensionless fracture length γ in these different limiting cases. The details of these solutions can be found in appendix A. The dimensionless opening and fluid fluxes profiles are similar for the different limiting flow regimes as can be seen in Fig. 7. The dimensionless fracture length and opening at the fracture inlet are listed in Table 5.

The range of validity of these limiting regimes which assume a given form of friction over the whole fracture extent can be established by comparing them to a numerical solution accounting for the complete evolution of the friction factor.

4 Complete numerical solution

In order investigate the transition from laminar to the turbulent regime, we need to account for the combined dependence of the friction factor on both Reynolds number and relative roughness. As previously mentioned, we use the model proposed by Yang and Dou (2010) which reproduces published experimental results for friction in pipes very well. In accounting for the complete dependence of friction on the Reynolds number and relative roughness, we resort to a numerical solution of the system of equations (2)-(7). We solve the system with a second order, non-oscillatory central (NOC) scheme introduced by Nessyahu and Tadmor (1990). The scheme is Riemann-solver free, which makes it fairly straightforward to

implement for the problem under consideration. A potential drawback is that the scheme is known to suffer numerical dissipation (see e.g. Kurganov and Tadmor (2000); Kurganov and Lin (2007)), especially for highly non linear problems such as the set of equations being solved here. We are using this scheme with an anti-diffusive correction recently introduced by Zia (2015). The numerical solver is validated in the laminar flow regime and a relative error of about 1 and 0.3 percent compared to the analytical solution of the fracture length and inlet opening evolution over close to four decades of time is obtained respectively (see Appendix B for details). With this numerical solver in hand, where the dependence of friction is computed using Yang and Dou (2010) model, we now explore deviation from the laminar flow regime when the inlet value $\mathcal{R}$ of the Reynolds number exceeds the critical value $\mathcal{R}_c \approx 1380$.

4.1 Smooth fracture case

The smooth fracture case corresponds to large time ($t \gg t_{R\to S}$) where the fracture relative roughness has negligible effect on turbulent flow (i.e. when the width is sufficiently large). Despite the fact that the smooth turbulent regime is most likely never reached in practice as $t_{R\to S}$ is very large (see section 3.1 for discussion), it is nevertheless enlightening to first discuss how the solution evolves in the zero roughness case (setting the characteristic roughness lengthscale k to zero in Yang and Dou (2010) model).

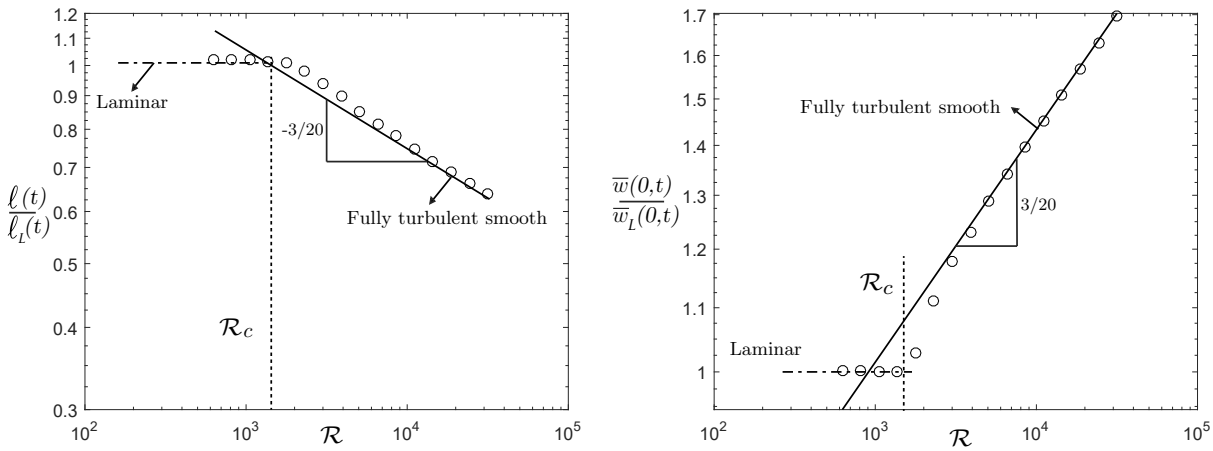

Figure 3: Fracture length $\ell(t)$ (left) and inlet width $\bar{w}(0,\, t)$ (right) relative to the fully laminar regime solution (ℓ_L, $\bar{w}_L$) as a function of the inlet Reynolds number $\mathcal{R}$: numerical results using Yang & Dou friction model (dots), fully turbulent smooth (continuous black line) and laminar (dashed dotted lines) limiting solutions. The relative difference with respect to the laminar solution as function of $\mathcal{R}$ can be directly seen in this plot.

In particular, from the scalings (Table 3), we can see that the solution (e.g. length, width) evolves with same power law of time as in the laminar case. We can therefore directly grasp the deviation from the fully laminar case by normalizing the numerical solution with the semi-analytical laminar solution. We have performed a series of simulations for different values of $\mathcal{R}$ in that smooth case. In Fig. 3, we display these numerical results of fracture length and inlet width normalized by the laminar solution for different values of $\mathcal{R}$. We have also displayed the semi-analytical solution obtained in the fully turbulent smooth regime (similarly scaled by the laminar solution). We observe that the numerical results tends to the fully smooth turbulent solution for $\mathcal{R} \gtrsim 5000$. In other words, the fully smooth turbulent solution is valid for $\mathcal{R}$ larger than 5000. The differences with the laminar solution can become very significant for large $\mathcal{R} > 10^4$, e.g. up to 40% for $\mathcal{R} = 10^4$.

The transition to the fully turbulent smooth regime can also be grasped by plotting the relative fraction of the fracture in the laminar regime, i.e. for which the local value of the Reynolds number ($Re_{D_{eq}} = \frac{5}{\pi}\mathcal{R}\Omega\Upsilon$) remains below the critical value. This laminar region is located near the fracture tip and shrinks to a boundary layer as $\mathcal{R}$ increases. This

can be clearly seen on Fig. 4. As soon as $\mathcal{R}$ goes above $\mathcal{R}_c \approx 1380$, the laminar fraction decreases fast until it falls below the spatial resolution of the simulation. It is important to note here that these simulations were performed with a grid of $N = 150$ cells which gives a dimensionless spatial resolution ($\xi = x/\ell$) of $1/N = 1/150 \approx 0.0066$. It is not a surprise that the numerical solution can not resolve the boundary layer below the grid size. From Fig. 4, we see that the laminar fraction is below 5 percent of the fracture length for $\mathcal{R} \approx 5000$. Our numerical results clearly demonstrate that the smooth turbulent regime is valid for $\mathcal{R} \gtrsim 5000$.

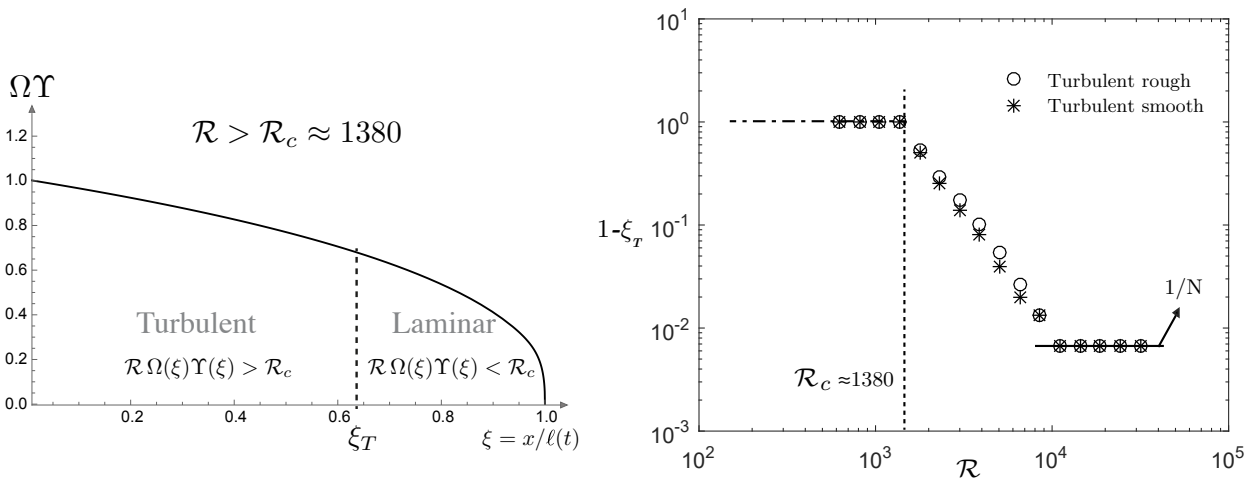

Figure 4: Sketch of the flow regimes along the fracture (plotting the dimensionless flux $\Omega\Upsilon$ along the fracture) for an entrance Reynolds number $\mathcal{R} = \dfrac{\rho Q_o}{2h\mu}$ above the critical value $\mathcal{R}_c$ (left). The relative extent $(1 - \xi_T)$ of the laminar region at the tip of the fracture decreases with increasing $\mathcal{R}$ above the transition to turbulent flow $\mathcal{R}_c$ (right).

4.2 Rough fracture

As previously discussed, in practice, fracture roughness will be dominant in the turbulent regime. The transition time scale to the turbulent smooth solution $t_{R\to S}$ is typically much larger than the injection duration in practice. It is therefore relevant to focus on the case of small time compared to $t_{R\to S}$. We perform a number of simulations for different $\mathcal{R}$, now also accounting for roughness in Yang and Dou (2010) model for injection duration much

smaller than $t_{R\to S}$. In these simulations, the domain is descretized with 150 cells and the parameters used are the same as in Table 1.

It is important to note that contrary to the smooth turbulent case, in the limit of rough turbulent flow (large $\mathcal{R}$) the solution evolves with a different power-law of time compared to the laminar case (see Table 3): 13/16 compared to 4/5 for fracture length, and 3/16 compared to 1/5 for fracture width respectively. In both the fully laminar ($\mathcal{R} < \mathcal{R}_c$) and fully turbulent rough ($\mathcal{R} \gg \mathcal{R}_c$) cases, the solution is self-similar. The propagation solution between these two limiting cases (away from the smooth limit) depends only on the value of the entrance Reynolds number $\mathcal{R}$. As $\mathcal{R}$ does not depend on time, it thus does not introduce any other time scale in the problem. For a given value of $\mathcal{R}$ within this transition, the corresponding numerical results exhibit a power-law dependence of time in-between the laminar and fully rough exponents.

In order to grasp the evolution of the propagation solution from the laminar to the rough turbulent regime, we write the fracture length and inlet width using the laminar solution at time $t = t_{R\to S}$ as characteristic scales:

$$\ell(t) = \underbrace{L_L(t_{R\to S})\gamma_L}_{\ell_L(t_{R\to S})} \times \sigma_\ell \tau^{\alpha_\ell}, \quad \bar{w}(0,t) = \underbrace{W_L(t_{R\to S})\Omega_L(0)}_{w_L(\xi=0,t_{R\to S})} \times \sigma_w \tau^{\alpha_w}. \tag{18}$$

where the dimensionless time $\tau = t/t_{R\to S}$ is defined with respect to the transition time-scale $t_{R\to S}$ from rough to smooth turbulent regime (the only time-scale appearing in the problem). $L_L(t_{R\to S})$ and $W_L(t_{R\to S})$ are the laminar characteristic length and width taken at $t = t_{R\to S}$ (see Table 3), and γ_L and Ω_L are the dimensionless fracture length and width in the laminar solution (see Tables 3,5 and appendix A). In equation (18), σ_ℓ, σ_w and α_ℓ, α_w are the pre-factors and power-law exponents of the fracture length (subscript ℓ) and width (subscript w) evolution respectively. For an entrance Reynolds number $\mathcal{R}$ below the critical one, the propagation is fully laminar such that $\sigma_\ell = \sigma_w = 1$, $\alpha_\ell = 4/5$ and $\alpha_w = 1/5$. For large $\mathcal{R}$ where the propagation is in the fully turbulent rough regime, from the solution in that limiting

regime (see the scaling in Table 3 and dimensionless solution Table 5) we obtain the corresponding limiting values: $\alpha_\ell = 13/16$, $\alpha_w = 3/16$ and $\sigma_\ell = L_R(t_{R\to S})\gamma_R/(L_L(t_{R\to S})\gamma_L) = 2.65\mathcal{R}^{-3/20}\gamma_R/\gamma_L \approx 2.85\mathcal{R}^{-3/20}$, $\sigma_w = W_R(t_{R\to S})\Omega_R(0)/(W_L(t_{R\to S})\Omega_L(0)) = 0.377\mathcal{R}^{3/20}\Omega_R(0)/\Omega_L(0) \approx 0.363\mathcal{R}^{3/20}$. One should also note that to tabulate the complete width profile $\bar{w}(x,t)$, one would have to introduce a dependence of σ_w with position (i.e. $\sigma_w(\xi)$). We only tabulate the inlet width in the following.

For a simulation with a given value of inlet Reynolds number $\mathcal{R}$, we obtain α_l, α_w and σ_ℓ, σ_w as the slope and intercept at the origin of the time evolution of fracture length/inlet width in log-log respectively. The results are listed in Table 4. These results provide values of σ and α as function of $\mathcal{R}$. The fracture length and inlet width can thus be conveniently evaluated using Eq. (18) for any value of $\mathcal{R}$. It is important to bare in mind that such a "tabulated" solution is valid only for time much smaller compared to the transition time-scale $t_{R\to S}$ to the turbulent smooth regime. The results tabulated in Table 4 are obtained by curve fitting of numerical data on at least two order of magnitude of dimensionless time ($\tau = t/t_{R\to S}$) in the range $\tau \approx 5\times 10^{-9}$ and $\tau \approx 5\times 10^{-7}$, a range of time relevant for most practical applications.

Table 4 shows that the parameters σ_ℓ, σ_w and α_ℓ, α_w attain values that are very close to the limiting rough turbulent solution for Reynold's numbers close to 10^4. This indicates that the limiting rough turbulent solution is valid for Reynolds number larger than 10^4. In the range $\mathcal{R} \in [2000-5000]$ relevant for hydraulic fracturing treatment, the solution is always in between the laminar and fully rough regime.

From these results, the departure of the complete solution from the laminar case can be grasped by dividing it by the laminar solution, i.e. $\sigma_\ell\tau^{\alpha_\ell-4/5}$ for the fracture length and $\sigma_w\tau^{\alpha_w-1/5}$ for the inlet racture width respectively. These ratio indicates that the difference evolves with time, i.e. the two solutions scale with different power laws of time. To illustrate such difference, considering a hydraulic fracturing operation with an injection rate of 30 bbl/min ($\mathcal{R} \approx 3000$) with the parameters listed in Table 1, we observe that after two hours

$\mathcal{R}$	σ_ℓ	α_ℓ	σ_w	α_w	$\alpha_l + \alpha_w$
Laminar	1	4/5	1	1/5	1
1200	1.0212	0.8012	0.9955	0.1998	1.0011
2000	0.9743	0.8041	1.1237	0.1898	0.9939
3000	0.9067	0.8074	1.2060	0.1883	0.9958
4000	0.8690	0.8099	1.2611	0.1880	0.9979
6000	0.8220	0.8129	1.3392	0.1877	1.0006
10000	0.7491	0.8131	1.4491	0.1878	1.0009
30000	0.6021	0.8103	1.6800	0.1868	0.9971
Rough	$2.85\mathcal{R}^{-3/20}$	$13/16 = 0.8125$	$0.363\mathcal{R}^{3/20}$	$3/16 = 0.1875$	1
10000	0.7158	0.8125	1.445	0.1875	1

Table 4: Laminar-turbulent rough transition: pre-factors (σ_ℓ, σ_w) and exponents of the power-law (α_ℓ, α_w) for the fracture length and inlet width (Eq. (18)) for different value of the Reynold's number ($\mathcal{R}$). Note that in the absence of leak-off, for a constant injection rate, the fracture volume evolves linearly with time and scale as $\ell \times \bar{w} \times h$, such that we must always have $\alpha_\ell + \alpha_w = 1$, i.e. differences indicate the level of accuracy of our numerical scheme. The values for the limiting solutions in both the laminar and rough regimes are also listed. The numerical solution agrees with the rough turbulent solution for $\mathcal{R} \gtrsim 10,000$.

of injection the fracture length and the inlet width would be respectively 81 and 142 percents of the laminar solution.

As already discussed, the transition from the turbulent rough (small τ) to the turbulent smooth regime (large τ) takes an extremely long time for any realistic value of the characteristic roughness. It is of limited practical interest. We leave the numerical investigation of this transition to future work, and now focus on the more practically interesting effect of the addition of friction reducers in the fluid.

5 Effect of friction reducers

Polymer drag reducing agents are widely used in the hydraulic fracturing industry in order to reduce the friction in the wellbore caused by turbulence of the injected fluid. Without the addition of such friction reducers, the power required on-site for a slick-water treatment would be up to 80% larger. The molecules of these polymer additives consist of long chains of atoms which align themselves with the flow direction, suppressing eddies and thus reducing

turbulence. A small amount of such heavy-weight polymers is sufficient to completely change the transition to turbulence.

Starting from the pioneering work of Toms (1948), there have been numerous studies to estimate the reduction of drag by addition of heavy molecular weight polymers (see e.g. Lumley (1969); Virk (1975); Yang (2009); White and Mungal (2008)). This reduction can be quantified by estimating the decrease in the friction factor as the concentration of the friction reducing agent is increased. As discussed earlier, most of the data regarding friction factor is obtained from experiments performed on circular pipes. To the best of our knowledge, there is no experimental data available in non-circular pipes for different level of drag reducing agents and relative roughness. We use experimental data obtained on circular pipes with different relative roughness provided by Virk (1971). Virk notably showed that the effect of drag reducing agents saturate above a given concentration. In other words, there is a maximum drag reduction asymptote which is reached for a finite (and relatively low) concentration of the polymer. The experimental results of Virk (1971) are displayed on Fig. 5 for different relative roughness at maximum drag reduction together with the pure water results of Nikuradse (1950). The effect of friction reducer is striking. For smooth pipe, the transition to turbulence is completely different and the value of friction is much lower. The effect of pipe roughness is also much less significant, especially in the range of Reynolds number of interest for hydraulic fracturing applications ($\mathcal{R} \in [10^3 - 10^4]$). Focusing on this range of inlet Reynolds number, we can neglect any effect of relative roughness (see Fig. 5). For smooth pipes, Virk (1971) gives the maximum drag reduction (MDR) asymptote in the form of the following implicit function:

$$\frac{1}{\sqrt{f}} = 19 \log_{10}\left(\frac{Re_{D_{eq}}}{\sqrt{f}}\right) - 32.4. \tag{19}$$

In our case, the preceding formula can be used in combination with the equivalent Reynolds number (8) to accommodate the flow geometry. Moreover, in the range $\mathcal{R} \in [10^3 - 10^4]$, the

MDR asymptote can be conveniently approximated by the following explicit relation:

$$f = 1.78 Re_{D_{eq}}^{-0.7}. \tag{20}$$

It is interesting to note that it takes the form $f = f' Re^{-\beta}$ for which we have obtained a semi-analytical solution (assuming that friction follow this law over the entire fracture). To span the transition from laminar to the MDR asymptote (20), in our numerical simulations, we use a piece wise evolution of friction below (laminar) and above (MDR asymptote) the critical Reynolds number. Note that a slight jump in friction occur between these two regimes when using the approximation (20).

Similarly to the turbulent smooth case, since friction always evolve as $Re^{-\beta}$, the fracture length, width etc. evolves with the same power-law of time than the laminar case. The numerical results, for a given $\mathcal{R}$, when normalized by the laminar solution are thus constant in time. For a given value of $\mathcal{R}$, we run the simulation for several decades of time in order to check the self-similarity of the numerical results (i.e. the fact that the ratios $\ell(t)/\ell_L(t)$, $\bar{w}(x,t)/\bar{w}_L(x,t)$ are constant for a given $\mathcal{R}$). For a given $\mathcal{R}$, this normalized solution is constant up to numerical noise (10^{-3}) over the duration of the simulation (run typically for over three decades of time). The fracture length and width normalized by the laminar solution for different values of $\mathcal{R}$ are shown in Fig. 6, left and right respectively. It is interesting to note that the transition to the full maximum drag reduction solution happens fast. For $\mathcal{R} > 2000$, the numerical results are exactly similar to the semi-analytical MDR limiting solution. These results allow to directly grasp the relative difference between the propagation with friction reducer at maximum drag reduction concentration with the laminar solution. For $\mathcal{R} = 10^4$, the difference is about 10% and 15% for fracture length and inlet width respectively. A difference much smaller than the case without friction reducing agents (see e.g. Fig. 3 and 6). Neglecting the effect of drag reducing agents definitely results in very different results.

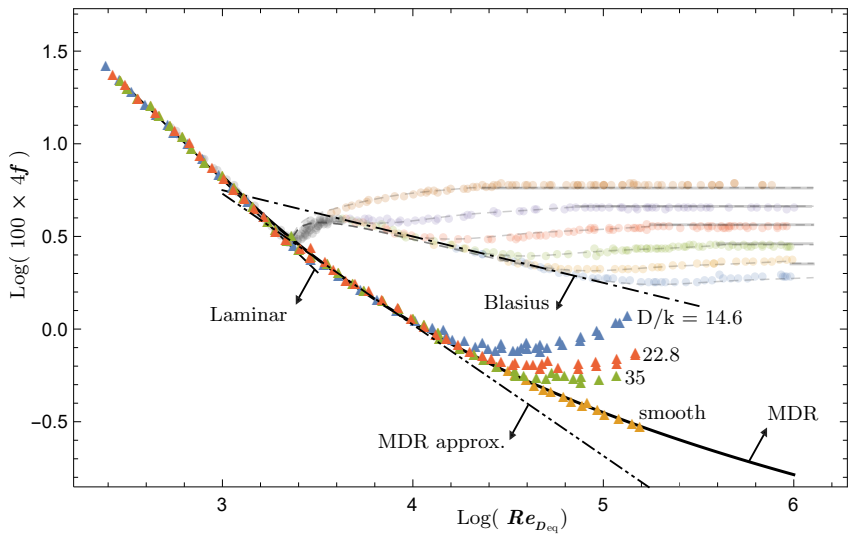

Figure 5: Friction factor as function of Reynolds number and relative roughness in pipes when friction reducing agents are added to water: data from Virk (1971), Virk's maximum drag reduction asymptote for smooth pipes (Eq. (19), continuous black line), and its approximation in the range $10^3 - 10^4$ (Eq. (20) in dashed dotted lines).

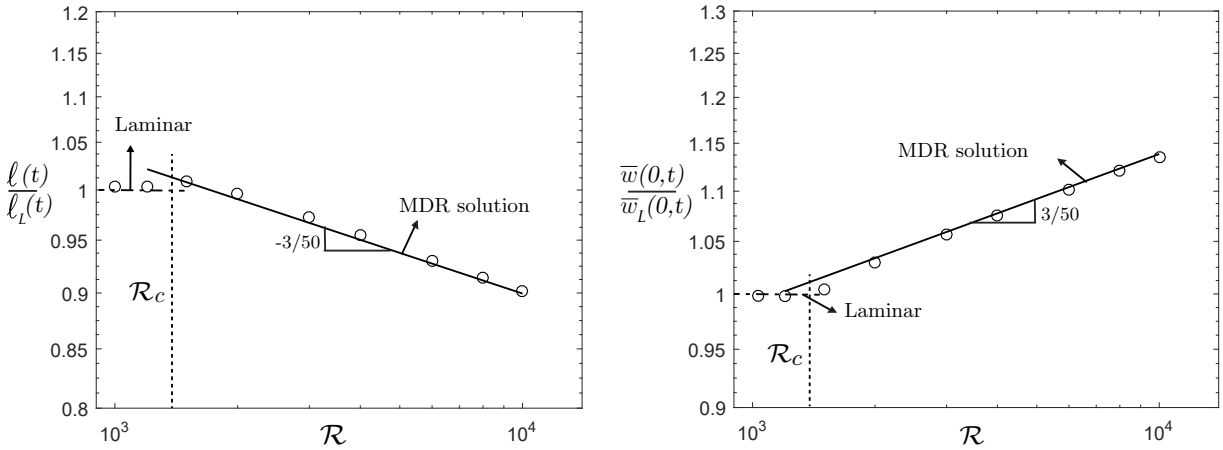

Figure 6: The fracture length $\ell(t)$ (left) and inlet fracture width $\bar{w}(0,\, t)$ (right) relative to the laminar solution as function of $\mathcal{R}$ when friction reducers are added in sufficient quantity to be at maximum drag reduction (MDR) in the turbulent regime: numerical results for the complete evolution of friction factor from laminar to MDR (dots), solution for friction at maximum drag (continuous black line), fully laminar solution (dashed lines).

6 Conclusions

We have investigated the effect of turbulent flow on the propagation of height contained (PKN) hydraulic fractures. The concept of equivalent laminar hydraulic radius (Jones, 1976) allows to use the friction factor relations $f(Re, w/k)$ obtained from experiments performed on circular pipes. A dimensional analysis of the problem has allowed to obtain a clear picture of the structure of the solution. First, we have seen that inertial effects will always be negligible in practice (confirming the a-posterio check of Tsai and Rice (2010) in plane-strain). We have also seen that when in the turbulent regime (pending the addition of friction reducing agents) the effect of the relative roughness governs friction and therefore fracture propagation for time smaller to a rough to smooth transition time-scale $t_{R\to S}$ (see Eq. (17)). For time larger than $t_{R\to S}$, the friction transition to the smooth turbulent regime (Blasius scaling Eq. (9)). For any practical cases and realistic value of the roughness lengthscale, such a transition time-scale will always exceed the injection duration.

For small time (compared to $t_{R\to S}$), our numerical results of hydraulic fracture propagation have shown that the semi-analytical solution for the limiting regime of turbulent rough friction (over the whole fracture) is valid for $\mathcal{R} \gtrsim 10000$. For lower value of the entrance Reynolds number $\mathcal{R}$, a tabulation of our numerical results allow to easily estimate the evolution of fracture length and inlet width according to Eq. (18) and Table 4, spanning the complete transition from laminar ($\mathcal{R} \lesssim 1380$) to turbulent rough ($\mathcal{R} \gtrsim 10000$). For large time (compared to this rough to smooth transition time-scale $t_{R\to S}$) roughness become negligible and turbulent flow is governed by Blasius scaling (i.e. smooth friction). Our numerical results indicate that the semi-analytical solution for the fully turbulent smooth friction is valid for $\mathcal{R} \gtrsim 5000$. In all cases (turbulent rough or smooth), the relative fraction of the fracture exhibiting laminar flow conditions is located at the fracture tip and its extent decreases with increasing $\mathcal{R}$ eventually reducing to a boundary layer (see Fig. 4). With respect to industrial applications where $\mathcal{R} < 5000$, we clearly see that the entrance Reynolds number is not sufficiently high for the fully turbulent solutions to be valid. Although our results have

been obtained for a height contained (PKN) hydraulic fracture, one can anticipate a similar trend for other fracture geometries: i) if turbulent, the flow inside the fracture will be in the turbulent rough regime for any realistic pumping duration and ii) the entrance Reynolds number $\mathcal{R}$ needs to be sufficiently large in order to approximate the flow as turbulent rough along the whole fracture and thus neglect the transition between fully rough turbulent flow at the fracture entrance to laminar flow near the fracture tip. A proper analysis for more complex fracture geometries would be needed in order to quantitatively confirm this. Comparison of the results presented in this paper with experimental data would be welcome to better assess the validity of the friction model used to describe the transition from laminar to turbulent flow in a fracture. It is however clear that achieving large Reynolds number in a fracture in the laboratory would be extremely difficult. A dedicated field experiment with a precise monitoring of the fracture length with time may be the best approach to test the solutions presented here.

We have also investigated the addition of friction reducing agents in sufficient concentration to be at the so-called maximum drag reduction asymptote (Virk, 1975). These friction reducers have obviously a first-order impact on the transition to turbulence and as a result on the propagation of height contained hydraulic fractures. We have obtained a semi-analytical solution in the limiting regime of maximum drag reduction over the entire fracture. Our numerical results accounting for the transition of friction from laminar to the MDR asymptote with $\mathcal{R}$ indicate that the limiting MDR regime solution is valid for $\mathcal{R} \gtrsim 2000$. The difference with the solely laminar solution remains below 10-15% for entrance Reynolds number $\mathcal{R}$ under 10^4. This directly indicates the error that one will make when designing a hydraulic fracturing treatment with the classical laminar solution (Nordgren, 1972) for a height contained (PKN) fracture. An error which has to be compared with the level of uncertainties on the rock and reservoir properties.

Acknowledgements This work was funded by the Swiss National Science Foundation (grant #160577).

References

Adachi, J., Detournay, E., 2002. Self-similar solution of a plane-strain fracture driven by a power-law fluid. International Journal for Numerical and Analytical Methods in Geomechanics 26 (6), 579–604.

Adachi, J. I., Peirce, A. P., 2008. Asymptotic analysis of an elasticity equation for a finger-like hydraulic fracture. Journal of Elasticity 90 (1), 43–69.

Ames, B. C., Bunger, A., 2015. Role of turbulent flow in generating short hydraulic fractures with high net pressure in slickwater treatments. In: SPE Hydraulic Fracturing Technology Conference. Society of Petroleum Engineers, SPE-173373-MS.

Blasius, H., 1913. Das Ähnlichkeitsgesetz bei Reibungsvorgängen in Flüssigkeiten. Springer.

Carlson, L., Irvine, T., 1961. Fully developed pressure drop in triangular shaped ducts. Journal of Heat Transfer 83 (4), 441–444.

Detournay, E., 2016. Mechanics of hydraulic fractures. Annual Review of Fluid Mechanics 48, 311–339.

Dontsov, E., Peirce, A., 2015. An enhanced pseudo-3d model for hydraulic fracturing accounting for viscous height growth, non-local elasticity, and lateral toughness. Engineering Fracture Mechanics 142, 116–139.

Economides, M. J., Nolte, K. G., 2000. Reservoir stimulation. Schlumberger, John Wiley & Sons.

Jones, O., 1976. An improvement in the calculation of turbulent friction in rectangular ducts. Journal of Fluids Engineering 98 (2), 173–180.

Kemp, L. F., et al., 1990. Study of nordgren's equation of hydraulic fracturing. SPE Production Engineering 5 (03), 311–314.

Kurganov, A., Lin, C.-T., 2007. On the reduction of numerical dissipation in central-upwind schemes. Commun. Comput. Phys 2 (1), 141–163.

Kurganov, A., Tadmor, E., 2000. New high-resolution central schemes for nonlinear conservation laws and convection–diffusion equations. Journal of Computational Physics 160 (1), 241–282.

Lamb, H., 1895. Hydrodynamics. Cambridge university press.

Lecampion, B., Desroches, J., 2015. Simultaneous initiation and growth of multiple radial hydraulic fractures from a horizontal wellbore. J. Mech. Phys. Sol. 82, 235–258.

Lecampion, B., Desroches, J., Weng, X., Burghardt, J., Brown, J. E., et al., 2015. Can we engineer better multistage horizontal completions? evidence of the importance of near-wellbore fracture geometry from theory, lab and field experiments. In: SPE Hydraulic Fracturing Technology Conference. Society of Petroleum Engineers.

Li, S., Huai, W., 2016. United formula for the friction factor in the turbulent region of pipe flow. PloS one 11 (5), e0154408.

Lister, J. R., Kerr, R. C., 1991. Fluid-mechanical models of crack propagation and their application to magma transport in dykes. Journal of Geophysical Research: Solid Earth 96 (B6), 10049–10077.

Lumley, J. L., 1969. Drag reduction by additives. Annual review of fluid mechanics 1 (1), 367–384.

Manneville, P., 2016. Transition to turbulence in wall-bounded flows: Where do we stand? Mechanical Engineering Reviews (0).

Nessyahu, H., Tadmor, E., 1990. Non-oscillatory central differencing for hyperbolic conservation laws. Journal of computational physics 87 (2), 408–463.

Nikuradse, J., 1950. Laws of flow in rough pipes. National Advisory Committee for Aeronautics Washington.

Nilson, R., 1981. Gas-driven fracture propagation. Journal of Applied Mechanics 48 (4), 757–762.

Nordgren, R., 1972. Propagation of a vertical hydraulic fracture. Society of Petroleum Engineers Journal 12 (04), 306–314.

Perkins, T., Kern, L., et al., 1961. Widths of hydraulic fractures. Journal of Petroleum Technology 13 (09), 937–949.

Sadatomi, M., Sato, Y., Saruwatari, S., 1982. Two-phase flow in vertical noncircular channels. International Journal of Multiphase Flow 8 (6), 641–655.

Sarvaramini, E., Garagash, D. I., 2015. Breakdown of a pressurized fingerlike crack in a permeable solid. Journal of Applied Mechanics 82 (6), 061006.

Sneddon, I., Elliot, H., 1946. The opening of a griffith crack under internal pressure. Quart. Appl. Math 4 (3), 262–267.

Spence, D., Turcotte, D., 1990. Buoyancy-driven magma fracture: A mechanism for ascent through the lithosphere and the emplacement of diamonds. Journal of Geophysical Research: Solid Earth 95 (B4), 5133–5139.

Toms, B. A., 1948. Some observations on the flow of linear polymer solutions through straight tubes at large reynolds numbers. In: Proceedings of the 1st International Congress on Rheology. Vol. 2. pp. 135–141.

Tsai, V. C., Rice, J. R., 2010. A model for turbulent hydraulic fracture and application to crack propagation at glacier beds. Journal of Geophysical Research: Earth Surface 115 (F3).

Virk, P., 1971. Drag reduction in rough pipes. Journal of fluid mechanics 45 (02), 225–246.

Virk, P. S., 1975. Drag reduction fundamentals. AIChE Journal 21 (4), 625–656.

White, C. M., Mungal, M. G., 2008. Mechanics and prediction of turbulent drag reduction with polymer additives. Annu. Rev. Fluid Mech. 40, 235–256.

Yang, B. H., Joseph, D. D., 2009. Virtual nikuradse. Journal of Turbulence (10), N11.

Yang, S.-Q., 2009. Drag reduction in turbulent flow with polymer additives. Journal of Fluids Engineering 131 (5), 051301.

Yang, S.-Q., Dou, G., 2010. Turbulent drag reduction with polymer additive in rough pipes. Journal of Fluid Mechanics 642, 279–294.

Zia, H., 2015. A numerical model for simulating sediment routing in shallow water flow. Ph.D. thesis, University of Geneva.

A Limiting regimes solutions

A.1 Laminar - turbulent smooth

When the friction factor is a sole function of Reynolds number of the type $f = f' R_{D_{eq}}^{-\beta}$, under negligible inertia, either in the laminar or turbulent smooth scalings (see Table 3) the dimensionless form of the governing equations (1)-(7) reduces to the following.

- Elasticity:

$$\Omega = \Pi,$$

- Continuity:

$$t\dot{\Omega} + \frac{1}{5}\Omega - \left(\frac{4}{5} + \frac{\dot{\gamma}}{\gamma}\right)\xi\frac{\partial\Omega}{\partial\xi} + \frac{1}{\gamma}\frac{\partial\Omega\Upsilon}{\partial\xi} = 0,$$

- Balance of momentum (neglecting the inertial term, $\mathcal{G}_\epsilon = 0$)

$$0 = -\frac{1}{\gamma}\frac{\partial\Pi}{\partial\xi} - (\Omega\Upsilon)^{-\beta}\frac{\Upsilon^2}{\Omega}$$

- Boundary conditions

$$\Omega(\xi = 0)\Upsilon(\xi = 0) = 1 \qquad \Omega(\xi = 1) = 0 \qquad \Omega(\xi = 1)\Upsilon(\xi = 1) = 0.$$

We therefore see that in such limiting regimes ($f = f' Re_{D_{eq}}^{-\beta}$), the dimensionless solution expressed in the proposed scalings does not depend on any dimensionless number indicating self-similarity of the solution. We conclude that the dimensionless functions γ, $\Pi = \Omega$ and Υ only depends on ξ: the time derivatives disappears, $\dot{\gamma} = \dot{\Omega} = 0$. First, we can rewrite the balance of momentum as:

$$\Omega\Upsilon = -\frac{\Omega^{\frac{3}{2-\beta}}}{\gamma^{1/(2-\beta)}}\left|\frac{\mathrm{d}\Omega}{\mathrm{d}\xi}\right|^{\frac{1}{2-\beta}-1}\frac{\mathrm{d}\Omega}{\mathrm{d}\xi}$$

The continuity equation combined with the balance of momentum thus simplifies to:

$$\frac{\Omega}{5} - \frac{4}{5}\xi\frac{\mathrm{d}\Omega}{\mathrm{d}\xi} + \frac{1}{\gamma}\frac{\mathrm{d}}{\mathrm{d}\xi}\left(-\frac{\Omega^{\frac{3}{2-\beta}}}{\gamma^{1/(2-\beta)}}\left|\frac{\mathrm{d}\Omega}{\mathrm{d}\xi}\right|^{\frac{1}{2-\beta}-1}\frac{\mathrm{d}\Omega}{\mathrm{d}\xi}\right) = 0.$$

Integrating the continuity equation from ξ to 1 and using the boundary conditions, we obtain the following non-linear ODE:

$$\int_{\xi}^{1}\Omega(\xi')\ \mathrm{d}\xi' + \frac{4}{5}\xi\Omega + \frac{\Omega^{\frac{3}{2-\beta}}}{\gamma^{1+1/(2-\beta)}}\left|\frac{\mathrm{d}\Omega}{\mathrm{d}\xi}\right|^{\frac{1}{2-\beta}-1}\frac{\mathrm{d}\Omega}{\mathrm{d}\xi} = 0. \tag{21}$$

The dimensionless global volume balance (i.e. obtained when $\xi = 0$) using the inlet flux boundary conditions gives:

$$\gamma\int_{0}^{1}\Omega(\xi')\mathrm{d}\xi' = 1. \tag{22}$$

Assuming $\Omega = (1-\xi)^{\alpha}$, close to the fracture tip (when $\xi \to 1$) and introducing such form in the previous equation (21), we can obtain the following exponent for the width tip asymptote:

$$\alpha = \frac{1}{2+\beta}.$$

Such an asymptotic behavior of the fracture width notably gives a finite fluid velocity at the tip.

Solution: Following Adachi and Detournay (2002), we write the fracture width as the following series expansion:

$$\Omega = \sum_{j=1}^{\infty} A_j\Omega_j^* + B\Omega^{**}, \tag{23}$$

where Ω_j^* are the following basis function:

$$\Omega_j^* = (1-\xi^2)^{\alpha}C_{2j-2}^{(\alpha+1/2)}(\xi).$$

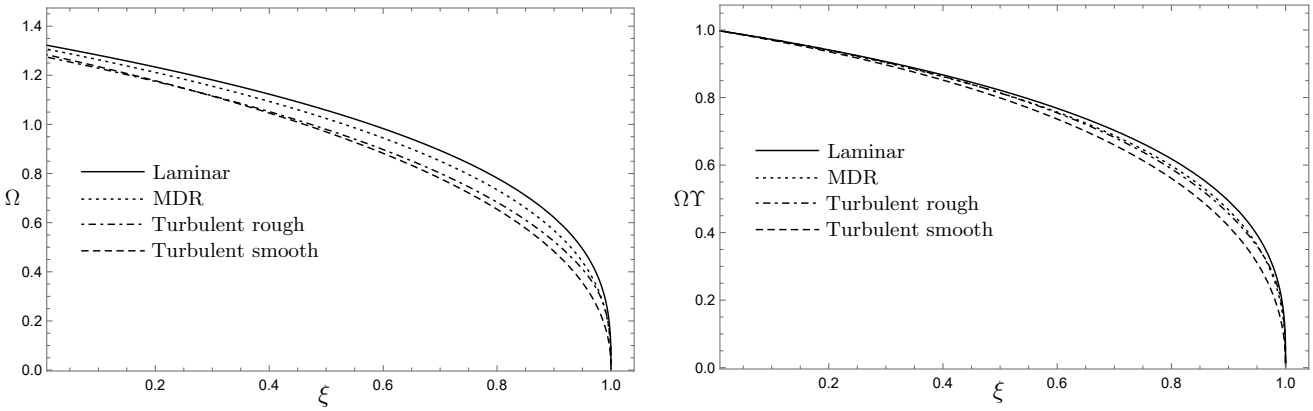

Figure 7: Dimensionless fracture width (Ω) and fluid flux ($\Omega \times \Upsilon$) for the laminar, turbulent smooth (Blasius) and turbulent rough (Gauckler-Manning-Strickler) limiting regimes.

C_b^a denotes the Gegenbauer polynomial of degree b and order a. Ω^{**} is a particular function chosen to reproduce the inlet behavior. Indeed,

$$\frac{\mathrm{d}\Omega_j^*}{\mathrm{d}\xi} = 2(\frac{1}{2} + \alpha)(1-\xi^2)^{\alpha} C_{2j-3}^{\alpha+3/2}(\xi) - 2\alpha\xi(1-\xi^2)^{\alpha-1} C_{2j-2}^{\alpha+1/2}(\xi)$$

is equal to zero at the inlet ($\xi = 0$). For simplicity, we choose:

$$\Omega^{**} = 1 - \xi,$$

to reproduce the inlet behavior. We truncate the series at $j = N_k$ to discretize the dimensionless continuity equation (21) together with the global volume balance (22). We use $N_c > N_k + 1$ collocations points regularly spaced in the interval $\xi \in [0, 1]$ to obtain N_c equations. We minimize the L_2 norm of the residuals $\|R\|_2$ of these N_c equations using Mathematica built-in optimizing algorithm (NMinimize function) with the constraints that $A_{j+1} < A_j < 0$. The corresponding dimensionless opening and fluid flux are shown in Fig. (7). The complete series coefficients, fracture length and inlet width are listed on Table 5.

	Laminar	Turbulent smooth	Turbulent rough	MDR
B	0.4288	0.513	0.477	0.4599
A_1	0.934	0.812	0.829	0.887
A_2	0.0434	$4.24\,10^{-2}$	$3.56\,10^{-2}$	$4.34\,10^{-2}$
A_3	$3.28\,10^{-3}$	$4.0\,10^{-3}$	$8.97\,10^{-3}$	$3.61\,10^{-3}$
A_4	$1.96\,10^{-3}$	$2.0\,10^{-3}$	$8.97\,10^{-3}$	$2.0\,10^{-3}$
A_5	$4.68\,10^{-4}$	$5.1\,10^{-4}$	$6.29\,10^{-3}$	$4.88\,10^{-4}$
A_6	$3.34\,10^{-4}$	$3.09\,10^{-4}$	$4.51\,10^{-3}$	$3.26\,10^{-4}$
A_7	$8.08\,10^{-5}$	$7.49\,10^{-5}$	$2.74\,10^{-3}$	$7.83\,10^{-5}$
A_8	$6.44\,10^{-5}$	$5.21\,10^{-5}$	$1.54\,10^{-3}$	$5.97\,10^{-5}$
A_9	-	-	$6.85\,10^{-4}$	-
A_{10}	-	-	$2.22\,10^{-4}$	-
Residuals $\|R\|_2$	$1.3\,10^{-6}$	$3.5\,10^{-7}$	$2.8\,10^{-6}$	$7.32\,10^{-7}$
γ	1.001	1.099	1.082	1.036
$\Omega(0)$	1.326	1.288	1.276	1.31

Table 5: Numerical coefficients of the dimensionless opening series (23) for the different limiting flow regimes. The corresponding dimensionless fracture length and inlet opening are also listed. The residuals obtained after numerical minimization are below 10^{-5} for all cases.

A.2 Rough turbulent regime - Gauckler-Manning-Strickler

In that limiting regime, friction is governed by the Gauckler-Manning-Strickler scaling $f = f'_M \left(\frac{k}{\overline{w}}\right)^{1/3}$. Neglecting inertia again ($\mathcal{G}_\epsilon \ll 1$) in the corresponding rough turbulent scaling (see Table 3), the dimensionless equations of the problem reduce to:

- Elasticity:

$$\Omega = \Pi,$$

- Continuity:

$$t\dot{\Omega} + \frac{3}{16}\Omega - \left(\frac{13}{16} + \frac{\dot{\gamma}}{\gamma}\right)\xi\frac{\partial\Omega}{\partial\xi} + \frac{1}{\gamma}\frac{\partial\Omega\Upsilon}{\partial\xi} = 0,$$

- Momentum:

$$\Omega\Upsilon = -\frac{\Omega^{5/3}}{\gamma^{1/2}}\left|\frac{\partial\Pi}{\partial\xi}\right|^{-1/2}\frac{\partial\Pi}{\partial\xi},$$

- and boundary conditions:

$$\Omega(\xi=0)\Upsilon(\xi=0)=1 \qquad \Omega(\xi=1)=0 \qquad \Omega(\xi=1)\Upsilon(\xi=1)=0$$

Similarly than for the laminar and smooth turbulent limiting regimes, we see that the dimensionless solution only depends on ξ in that limiting regime: the solution is self-similar. The continuity equation combined with the balance of momentum simplifies to:

$$\frac{3\Omega}{16}-\frac{13}{16}\xi\frac{\mathrm{d}\Omega}{\mathrm{d}\xi}+\frac{1}{\gamma}\frac{\mathrm{d}}{\mathrm{d}\xi}\left(-\frac{\Omega^{5/3}}{\gamma^{1/2}}\left|\frac{\mathrm{d}\Pi}{\mathrm{d}\xi}\right|^{-1/2}\frac{\mathrm{d}\Omega}{\mathrm{d}\xi}\right)=0.$$

Integrating the continuity equation from ξ to 1 and using the boundary conditions, we obtain the following non-linear ODE:

$$\int_{\xi}^{1}\Omega(\xi')\ \mathrm{d}\xi'+\frac{13}{16}\xi\Omega+\frac{\Omega^{5/3}}{\gamma^{3/2}}\left|\frac{\mathrm{d}\Omega}{\mathrm{d}\xi}\right|^{-1/2}\frac{\mathrm{d}\Omega}{\mathrm{d}\xi}=0. \tag{24}$$

Assuming $\Omega=(1-\xi)^{\alpha}$ when $\xi\to 1$ and introducing such form in the previous equation (24), we obtain here $\alpha=3/8$ for the exponent of the opening tip asymptote. The solution is obtained using the same numerical method than for the previous cases. The dimensionless opening and flux profiles can be seen in Fig.7, all the numerical values of the series coefficient in Table 5.

B Verification of the numerical solver

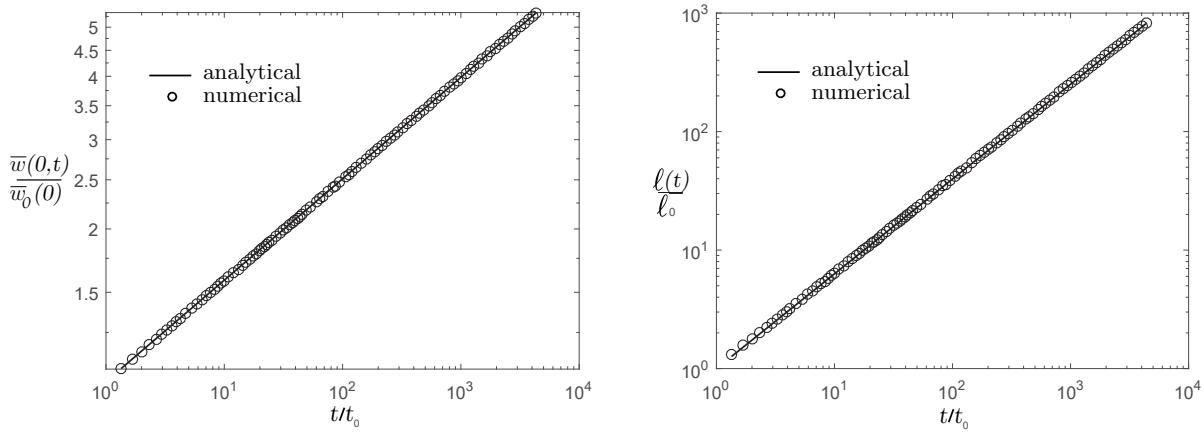

Figure 8: Fully Laminar Case ($f = 16/Re_{D_{eq}}$): Evolution with scaled time of the fracture length (right) and fracture width at the fracture inlet (left).

In order to demonstrate the accuracy of the numerical scheme, we compare our numerical results to the fully laminar analytical solution (Kemp et al., 1990) using only the laminar expression of the friction factor ($f = 16/Re_{D_{eq}}$) in our scheme. The numerical solution is obtained by discretizing the domain with a fixed Cartesian mesh of 150 cells. A re-meshing is performed as soon as the fracture tip reaches the end of the computational domain. The time step is evaluated with the following CFL (Courant-Friedrich-Lewy) condition:

$$\triangle t = C_n \, \frac{\Delta x}{\max\{\lambda\}},$$

where $C_n = 0.01$ is the courant number, $\lambda = \overline{v}(x) \pm \sqrt{p/\rho}$ is the "wave speed" given by the eigenvalues of the Jacobian of the set of Equations (4) and (7), and Δx is the cell size. To locate the fracture tip, we characterize the fracture as open at the point along the fracture length where the opening goes above a small threshold value (taken here as 4 percent of the fracture width at the inlet). The fracture tip is assumed to be propagating with a constant velocity while the tip remains in a cell, i.e. the fracture width in the adjacent cell is increasing with the time but is below the threshold. The velocity is re-evaluated each time the width

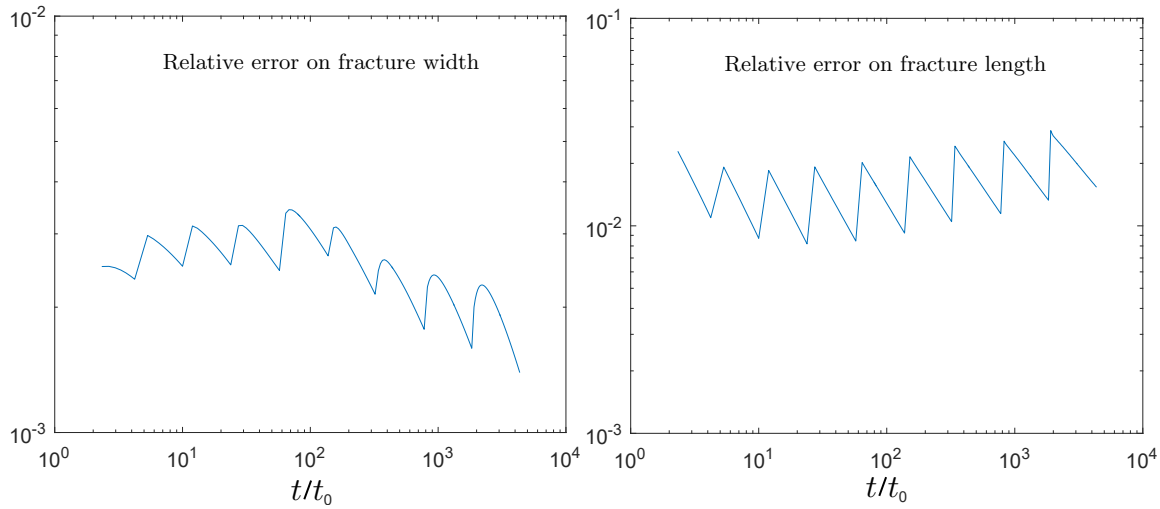

Figure 9: Fully Laminar Case ($f = 16/Re_{D_{eq}}$): Evolution with scaled time of the Relative error in percentage of the numerical solution for fracture-length (right) and fracture-width (left).

goes above the threshold and the tip enters the adjacent cell. To mitigate the numerical diffusion of the scheme, a large value of 0.999 for the correction factor ϵ (see Zia (2015) for description of this correction parameter) is used. Other parameters used for this numerical run are the one listed in Table 1 with an injection rate of $Q_0 = 0.015$ m^3/s.

The simulation is started with the Initial conditions prescribed as the exact laminar solutions ($w_0(x) = w(x, t_0)$ and $\ell_0 = \ell(t_0)$) at a given initial time t_0 (2 seconds in this test case) and the solution is allowed to evolve with time. Figure 8 shows the evolution of the scaled fracture-length $\ell(t)/\ell_0$ vs scaled time (t/t_0) and the scaled fracture-width at the inlet $w(0, t)/w_0$ vs scaled time (t/t_0) on right and left respectively. A very good match with the analytical solutions can be observed. Furthermore, the relative error of the fracture-length and the fracture-width are shown in Fig. 9 on the right and left respectively. The sharp jumps in the time evolution of the error are due to re-meshing which is performed as the fracture tip reaches the end of the computational domain. This introduces a small error due to the loss of data caused by interpolations. However, as Fig. 9 shows, this error accumulation is not significant. The relative errors for the fracture width and fracture length remain close to 0.3 and 2 percent respectively over more than three decades of time. Note that Figures 8 and 9

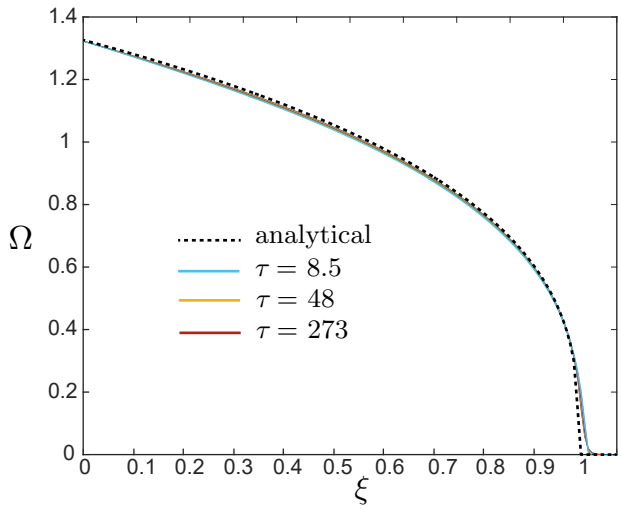

Figure 10: Fully laminar case ($f = 16/Re_{D_{eq}}$): Analytical and numerical solutions for dimensionless fracture width at different scaled times $\tau = t/t_0$. The small numerical diffusion observed at the fracture tip does not grow in time and is intrinsically related to the corrected adNOC scheme used here. It can be seen that the numerical solutions matches very close to the analytical solution and are indistinguishable from each other. (color online)

show the width at the fracture inlet only. The complete profile of the dimensionless fracture width (Ω) against the dimensionless fracture length (ξ) at different values of the scaled time ($\tau = t/t_0$) is shown in Fig. 10. The numerical solution matches the analytical solution very well, apart from a small diffusive region at the fracture tip which does not appear to "grow" in time.